

Article

Effect of Roughness on Conservative Solute Transport through Synthetic Rough Single Fractures

Zhou Chen ^{1,2,*} , Hongbin Zhan ³, Guiqing Zhao ¹, Yong Huang ¹ and Yefei Tan ⁴

¹ School of Earth Science and Engineering, Hohai University, Nanjing 210098, China; zhaogq@hhu.edu.cn (G.Z.); hyong38@gmail.com (Y.H.)

² Department of Civil Engineering, University of Toronto, 35 St. George Street, Toronto, ON M5S 1A4, Canada

³ Department of Geology and Geophysics, Texas A&M University, College Station, TX 77843, USA; zhan@geos.tamu.edu

⁴ Nanjing Hydraulic Research Institute, 225 Guangzhou road, Nanjing 210029, China; tan8112@gmail.com

* Correspondence: chenzhoucly@hhu.edu.cn; Tel.: +86-138-1541-8015; Fax: +86-025-8378-7234

Received: 31 July 2017; Accepted: 29 August 2017; Published: 1 September 2017

Abstract: Understanding solute transport in fractured rocks is of particular importance in many applications. Aperture values ranging from 4.7 to 8.7 mm and Reynolds number (R_e) values at 9.38~1743.8 were set for investigating fluid flow through synthetic horizontal single smooth and rough fractures. The Brilliant Blue FCF dye was chosen as the tracer to visualize the transport process. This paper focuses on the dispersion process in rough single fractures under non-Darcian flow conditions. Non-Darcian flow existed in both smooth and rough single fractures and the average flow velocity–hydraulic gradient (V – J) relationships were best described by the Forchheimer equation. The main objectives were to check the existing flow and transport models and to study possible correlations between fitting parameters and heterogeneities. The classical advection dispersion equation (ADE) model failed to capture the long-tailing of breakthrough curves (BTCs). Instead, the continuous time random walk (CTRW) model was better at explaining BTCs in both smooth and rough fractures, especially in capturing the long-tailing feature. The non-Darcian coefficient β_c in the Forchheimer equation and the coefficient β in the CTRW model appeared to be most relevant for characterizing the heterogeneity of the rough single fractures.

Keywords: rough single fracture; solute transport; non-Darcian; non-Fickian; heterogeneity

1. Introduction

The management of groundwater resources and control of contaminated aquifers require an understanding of the processes of flow and transport in porous or fractured rocks [1–5]. Fractures and bedding planes or faults give rise to preferential flow paths for groundwater, pollution in dilution, and free product, and thus are of great concern [6].

A single fracture has been traditionally idealized as parallel plates to obtain a tractable description of fluid flow and solute transport, and the model used to describe fluid flow in such an idealized single fracture is the local cubic law (LCL), which is essentially the expression of Darcy's law for a single fracture [7]. Also, Fickian transport is believed to be the "right" form of governing law for transport in the subsurface, where the dispersive mass flux is assumed to be proportional to the first derivative of the resident solute concentration [8]. However, real fractures have rough walls with points of contact, in which the transport is found to be non-Fickian on many occasions [1,2,7]. In general, there are two distinctive features of non-Fickian transport. First, the peak value of a breakthrough curve (BTC) originated from a pulse input of a contaminant or tracer arrives earlier than expected from the advection dispersion equation (ADE) (early arrival). The early arrival often suggests one or multiple preferential paths for the solute transport. Second, the tailing of the BTC lasts much longer

than expected (the long tail) [2]. The long tail phenomena can possibly be interpreted in terms of: a multi-rates mass exchange process between mobile and immobile domains [9,10]; fracture wall roughness [11]; the absorption of solute on fracture walls [12,13]; a permeable rock matrix [14]; and the entrapment of solute in eddies inside the fracture [15–17].

There have been several attempts to seek an explanation for non-Fickian transport in single fractures. These include the continuous time random walk (CTRW) [18–22]; the fractional advection dispersion equation (FADE) [23]; the mobile–immobile approach (MIM) [7,24,25]; and the boundary layer dispersion [26]; among others.

Bauget and Fourar [1] and Nowamooz et al. [27] studied the solute transport in a transparent replica of a real single fracture and found that the Fickian ADE was incapable of modeling the heavy (or long) tails' behavior. Alternatively, CTRW was able to describe the non-Fickian dispersion. The influence of surface roughness on nonlinear flow behaviors in three-dimensional (3D) self-affine rough single fractures was determined by Wang et al. [28] using Lattice Boltzmann simulations. Non-Fickian transport through two-dimensional (2D) rough single fractures was numerically studied by Wang and Cardenas [29], and their results clearly showed early arrival and heavy tailing in BTCs. The degree of deviation of transport from Fickian to non-Fickian is captured by the parameter β of the truncated power law used in CTRW. Specifically, β was found to be proportional to fracture heterogeneity [1,24].

On the other hand, non-Darcian flow, which can arise in a number of different ways, may have a great impact on solute transport. Non-Darcian flow is particularly prone to occurring in heterogeneous geological formations such as in a single fracture [11,30–32] or in a fractured network [33] due to relatively high speeds of flow.

To investigate solute transport under non-Darcian flow conditions, Qian et al. [8] established a well-controlled physical model with a vertical smooth parallel fracture, and the non-Fickian transport process was identified with early arrival and long tails. A MIM model fitted both peak and tails of the observed BTCs better than the ADE model. On the basis of this experience, with the purpose of describing solute transport under different flow velocities and fracture apertures, Chen et al. [34] carried out a series of flow and tracer test experiments on an artificial channeled single fracture—a single fracture with contact in certain areas—constructed in the laboratory. The flow condition showed a non-Darcian feature (best described by the nonlinear Forchheimer equation) and BTCs showed a non-Fickian feature such as early arrival of the peak value, long tailing and multi-peak phenomena. The results of this study [34] showed that ADE was not adequate to describe BTCs.

In a similar way to that undertaken by the study of Chen et al. [34], laboratory flow and tracer tests have been carried out on an artificially created fractured rock sample by Cherubini et al. [7], which showed a Forchheimer type of non-Darcian flow, and profound mobile–immobile mass exchange in terms of transport.

The main goals here were to test different models on the solute transport through a rough single fracture under non-Darcian flow conditions and to study possible correlations between fitting parameters and fracture heterogeneities. With these objectives in mind, the following tasks were carried out in sequence. First, synthetic rough single fractures with different roughness elements were designed. Then a series of flow and tracer test experiments were performed with a Reynolds number (Re) ranging from 9.38 to 1743.8. An imaging process was introduced to obtain a precise 2D concentration distribution for visual inspection. Subsequently, the characteristics of BTCs were analyzed and two models (ADE and CTRW) tested for their capacity to characterize the non-Fickian transport behavior under non-Darcian flow conditions.

2. Theory

2.1. Flow Model

Generally the model used to describe fluid flow in fractured media is LCL, which adapts Darcy's law [35]:

$$J = -\frac{\mu}{K\rho g}V = -kV, \quad (1)$$

where J is the hydraulic gradient [dimensionless], K is the hydraulic conductivity [m/s], μ is dynamic viscosity [mPa s], ρ is water density [kg/m³], g is the gravitational acceleration [m/s²], V is flow velocity [m/s] and k is the Darcian coefficient. A minor note is that porosity in a single fracture is expected to be 1, meaning that there is no filling materials inside the single fracture.

When a nonlinear flow feature occurs, the flow models commonly used to represent non-Darcian flow behavior are the Forchheimer law and the Izbash law. The former includes a quadratic term of velocity to represent the inertial effect [36,37]:

$$J = -\left(\frac{\mu}{K\rho g}V + \frac{\beta_c}{g}V^2\right) = -(aV + b_cV^2) \quad (2)$$

where β_c [m⁻¹] is the inertial term friction coefficient or non-Darcian coefficient, and a [s/m] and b_c [s²/m²] are the linear and inertial coefficients, respectively. If $b_c = 0$, flow becomes Darcian. If $a = 0$, flow becomes fully developed turbulent [30].

The Izbash law, or the power-law, equation is as follows [35]:

$$J = -cV^m \quad (3)$$

where c [s²/m²] and m [dimensionless] are two constant coefficients. The Forchheimer and Izbash equations are equivalent when $a = 0$ in Equation (1) and $m = 2$ in Equation (2).

Another dimensionless parameter to analyze the inertial versus viscous forces is the Reynolds number (R_e), which is defined as [30]:

$$R_e = \frac{2Vb}{\nu} \quad (4)$$

where b is the fracture aperture [mm], and ν is the kinematic viscosity of water [mm²/s] (here $\nu = 1.308$ mm²/s at 10 °C).

The V - J relationships obtained by experiments were fitted by the utility Cftool in Matlab. The quality of the fitting was discussed based on the decision coefficient r^2 , the error squared SSE, and the root mean square error (RMSE), as:

$$r^2 = 1 - \frac{\sum_{i=1}^N (J_{i0} - J_{ie})^2}{\sum_{i=1}^N (J_{i0} - \bar{J}_{i0})^2} \quad (5)$$

$$SSE = \frac{1}{N} \sum_{i=1}^N (J_i - \bar{J}_i)^2 \quad (6)$$

$$RMSE = \sqrt{\frac{1}{N} \sum_{i=1}^N (J_{ie} - \bar{J}_{i0})^2} \quad (7)$$

where J_i is the i th hydraulic gradient, \bar{J}_i is the average hydraulic gradient, J_{ie} is fitted hydraulic gradient, J_{i0} is the test hydraulic gradient, \bar{J}_{i0} is the average test hydraulic gradient, N is the number of the test hydraulic gradients.

2.2. The Advection Dispersion Approach

The general formation of the well-known ADE for a conservative solute without any sink/sources in a one-dimensional framework is given as,

$$\frac{\partial C}{\partial t} + V \frac{\partial C}{\partial x} = D \frac{\partial^2 C}{\partial x^2} \quad (8)$$

where C is the average solute concentration, D is the longitudinal hydrodynamic dispersion coefficient, t is time, and x is distance from the injected position along the flow direction. An analytical solution of Equation (8) with an instantaneous injection of tracer is [38]:

$$C(x, t) = \frac{M/A}{2\sqrt{\pi Dt}} e^{-\frac{(x-Vt)^2}{4Dt}} \quad (9)$$

where M is the injected mass, A is the cross-sectional area of the fracture over which injection occurs. The tracer is assumed to be injected uniformly over the entire saturated thickness of the fracture.

2.3. Continuous Time Random Walk

The continuous time random walk theory (CTRW) has been developed specifically to model the non-Fickian tracer transport [1,39–42]. The CTRW transport equation is based on the Fokker-Planck equation with a memory equation (FPME) which originally describes the temporal evolution of the probability density function of the velocity of a particle under the influence of drag and random forces. In CTRW, the Laplace transformed concentration function $\tilde{C}(x, w)$, is given by the one-dimensional form of FPME,

$$w\tilde{C}(x, w) - C_0(x) = -\tilde{M}(w)[u_\psi \frac{\partial}{\partial x} \tilde{C}(x, w) - D_\psi \frac{\partial^2}{\partial x^2} \tilde{C}(x, w)] \quad (10)$$

where w is the Laplace variable, and u_ψ and D_ψ are transport velocity and dispersion in the framework of CTRW respectively. In Equation (10), the memory function $\tilde{M}(w)$ captures the anomalous or non-Fickian transport induced by local heterogeneity or process and the corresponding formulation is given by

$$\tilde{M}(w) = \bar{t}w \frac{\tilde{\psi}(w)}{1 - \tilde{\psi}(w)} \quad (11)$$

where \bar{t} is some characteristic time and $\tilde{\psi}(w)$ is the transition rate probability, which is the core of the CTRW model. In general, there are three different models for $\tilde{\psi}(w)$, the asymptotic model, the truncated power law (TPL) model, and the modified exponential model. Details for the three different models of $\tilde{\psi}(w)$ can be found in the reference Cortis and Berkowitz [18]. Here, the most-used TPL model was adopted in the framework of CTRW,

$$\tilde{\psi}(w) = (1 + \tau_2 w t_1)^\beta \exp(t_1 w) \frac{\Gamma(-\beta, \tau_2^{-1} + t_1 w)}{\Gamma(-\beta, \tau_2^{-1})} \quad (12)$$

where t_1 represents the lower limit time when the power law behavior begins, t_2 is the cut-off time describing the Fickian behavior, and $\Gamma(\cdot)$ represents the incomplete Gamma function. The parameter β indicates different types of anomalous transport. Following Berkowitz et al. [40], $\tilde{\psi}(w)$ may be approximated by a power-law decay function, $t^{-1-\beta}$, where β is a parameter that characterizes dispersion. For $\beta > 2$, the process is Fickian and CTRW is equivalent to the classical ADE model. If $2 > \beta > 1$, the process is no longer Fickian and shows moderately anomalous transport; If $1 > \beta > 0$, the process indicates highly anomalous transport.

3. Experimental Results

3.1. Experiment Setup and Test Process

Artificial horizontal single fractures were constructed in the laboratory using organic glass plates, as per the schematic shown in Figure 1a. Although such artificial single fractures may not represent all the features of natural fractures, excellent control of flow field can be imposed on the apparatus, and the influence of roughness on water flow through single fractures can be studied in great detail. A detailed setup can be found in Chen et al. [11]. Three different kinds of roughness were used for the upper wall (Figure 1b): a smooth parallel plate; a rough plate with rectangular rough elements; and a rough plate with trapezoidal rough elements. For each type of rough single fractures, four types of asperity heights (Δ), including 2 mm, 4 mm, 6 mm and 8 mm, were used. The corresponding relative roughness (ϵ), which equals the ratio of Δ and the maximum aperture b_{\max} (10 mm), were 0.2, 0.4, 0.6 and 0.8 respectively. Therefore, the average apertures (b_a), which equal the average asperity heights of the rough single fracture (calculation shown in Figure 1b), were obtained and shown in Table 1.

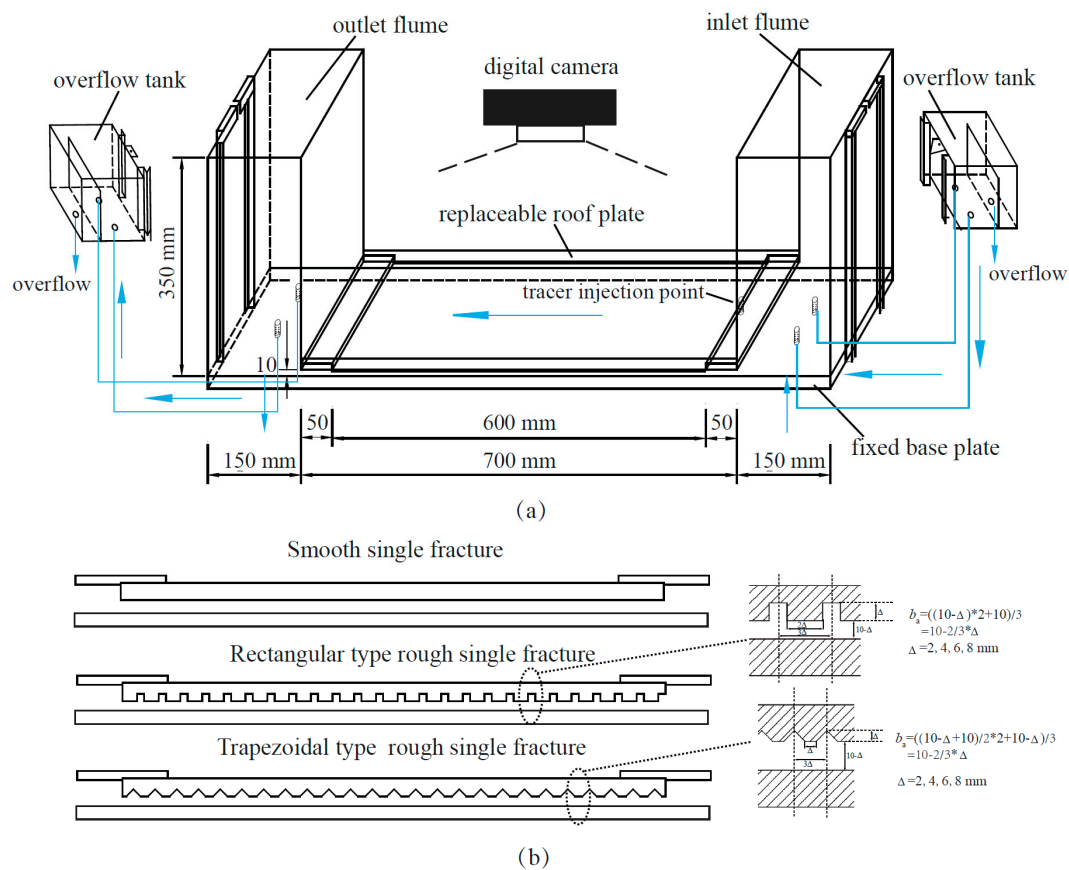


Figure 1. Schematic figure of the experimental setup.

Table 1. Average aperture and relative roughness for different single fractures.

Roughness Element	Average Aperture b_a (mm)				Relative Roughness ($\epsilon = \Delta/b_{\max}$)			
	A	B	C	D	A	B	C	D
Smooth	4.7	6.0	7.3	8.7				
Trapezoidal	4.7	6.0	7.3	8.7	0.8	0.6	0.4	0.2
Rectangular	4.7	6.0	7.3	8.7	0.8	0.6	0.4	0.2

The water levels at the recharge and discharge reservoirs were measured using piezometers with errors less than 0.5 mm. The hydraulic gradient through the single fracture was controlled through adjusted water levels between the inflow and the outflow reservoirs. The average flow rate was monitored using a calibrated flow meter LZB-25 (glass Rotameter made by Chengfeng Flowmeter Co. Ltd., Changzhou, Jiangsu, China) with a maximum permissible error of 1.5%. The average velocity was calculated by the average flow rate divided by the average aperture and width of the fracture. The flow experiments under different hydraulic gradients were carried out for a given single fracture. After that, the upper plate was replaced by a plate with a different type of roughness, and the entire flow experiment was repeated.

The dye Brilliant Blue FCF (bis [4-(*N*-ethyl-*N*-3-sulfophenylmethyl) aminophenyl]-2-sulfophenyl methylum disodium salt) was chosen as the tracer here for visual inspection and image process. It is important to choose an appropriate tracer concentration. If the selected concentration is too high, the gravity and density of the tracer may be a concern. If the concentration is too low, it may not generate images of tracer transport that are of sufficiently high quality for visual inspection. Concentration of the dye Brilliant Blue FCF was set as 1200 mg/L after a series of preliminary tests. Instantaneous tracer was adopted using an injection syringe and 1 mL tracer was injected in each test. The tracer injection point was illustrated in Figure 1a.

The digital camera (Canon EOS 500D) was fixed on a tripod. The length of the camera lens from the main body of the single fracture was set about 650 mm. A light source was placed under the fracture and the light emitted by the lamp was evenly distributed over the transparent plexiglas plate of the main fracture. All tracer tests were carried out in a home-made digital darkroom and the only light source during the test was provided by the lamp.

3.2. Image Process

Image analysis was improved to the extent that estimation of dye concentration from soil color was possible [43]. The main purpose here was to analyze the color information in the image to obtain the mathematical relationship between the color and concentration, and to further analyze the temporal and spatial variation of the concentration. The main factors that affect the color of the image during the test are the intensity of the light source, the color temperature, and the camera's parameter settings (mainly the exposure and white balance). In order to ensure the accuracy of the digital image's color, color temperature adjustment is needed for each photo.

In this study, the water-filled fracture image was used as the background of each tracer test. The background image was subtracted from the image containing the tracer using the image subtract code by Matlab software. The result is shown in Figure 2. The residual color of the fracture surface caused by the dye tracer was reduced.

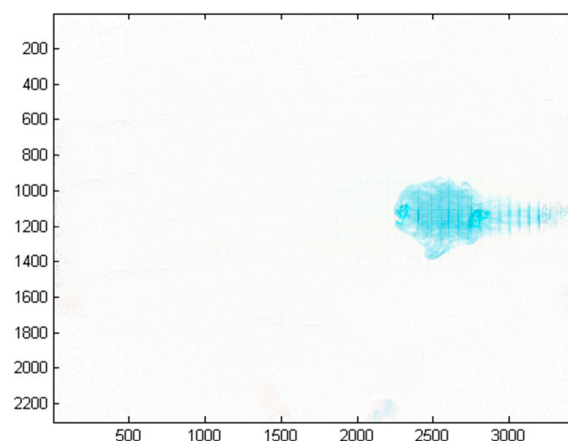


Figure 2. Difference in value between the adjusted image and the background image.

The RGB color model is the most commonly used on digital cameras. We tested the relationship of red (R), green (G), and blue(B) values and the concentration and finally found that the R value in the RGB model had the strongest correlation with the concentration [44].

The polynomial fitting of the relationship between the R value of the image and the concentration C was performed with a coefficient of determination of $r^2 = 0.990$ and RMSE = 0.757. The high r^2 value and the relatively low RMSE value suggested that the image processing method was acceptable.

Different fracture thickness and roughness for each test meant that the color of the same concentration solution in the medium was different. Therefore, the C–R relationships for each roughness type were obtained and the results were shown in Table 2, where the concentration has a unit of mg/L.

Table 2. The concentration C–R value equations for different single fractures (unit of C is mg/L).

Roughness Element	C–R Relation Equation	r^2
Rectangular A	$C = 0.0010 \times R^2 - 0.6442 \times R + 97.31$	0.995
Rectangular B	$C = 0.0007 \times R^2 - 0.3693 \times R + 50.92$	0.998
Rectangular C	$C = 0.0012 \times R^2 - 0.8386 \times R + 133.6$	0.990
Rectangular D	$C = 0.0007 \times R^2 - 0.3693 \times R + 50.92$	0.998
Trapezoidal A	$C = 0.003 \times R^2 - 1.670 \times R + 230.9$	0.992
Trapezoidal B	$C = 0.0014 \times R^2 - 0.9311 \times R + 144.2$	0.993
Trapezoidal C	$C = 0.0003 \times R^2 - 0.3572 \times R + 67.70$	0.992
Trapezoidal D	$C = -0.0006 \times R^2 - 0.101 \times R + 67.78$	0.995
Smooth A	$C = -0.0008 \times R^2 + 0.0506 \times R + 34.98$	0.990
Smooth B	$C = 0.0007 \times R^2 - 0.6243 \times R + 107.4$	0.991
Smooth C	$C = 0.0014 \times R^2 - 0.7719 \times R + 106.6$	0.992
Smooth D	$C = 0.0008 \times R^2 - 0.489 \times R + 74.03$	0.991

3.3. Flow and Tracer Experiments

The present works focused on relatively low velocity and small aperture. In order to investigate the tracer test in non-Darcian flow conditions, we chose a medium aperture ranging from 0.0047 to 0.0087 m and the Reynolds number (Re) at 9.38~1743.8. The evidence of non-Darcian flow is reflected in the nonlinear relationship between the hydraulic gradient and the flow rate at the given range of Re .

To analyze the characteristics of solute transport through single fractures more accurately, instantaneous tracer tests using the dye Brilliant Blue FCF were performed. The horizontal fractures with smooth parallel plates, rectangular cross-section rough fractures, and trapezoidal cross-section rough fractures, were chosen. For demonstration purposes, concentrations at position $x = 555$ mm downstream from the point of injection, which is located at the middle elevation at $x = 0$ mm, were calculated under flow velocity of 9.7 mm/s and 51.7 mm/s for smooth parallel plates; 44.3 mm/s and 71.0 mm/s for rectangular cross-section rough fractures; and 20.5 mm/s and 51.2 mm/s for trapezoidal cross-section rough fractures; and the results can be found in Figures 3–5 respectively.

A few observations can be made about Figure 3. For the smooth parallel plates shown in Figure 3, when flow velocity V was as small as 9.7 mm/s, the solute plume moved forward as a lump, but the color inside the plume for each point was not the same, indicating that the solute had not yet fully mixed. The front of the plume showed a typical Gaussian distribution. Lateral dispersion was also clearly visible and irregular movement of the solute with a long tail occurred. When the flow velocity V reached a relatively higher value of 55.1 mm/s, the front of the plume also showed a Gaussian distribution but the lateral dispersion was reduced. Similarly, with that for V of 9.7 mm/s, the concentration inside the plume showed apparent difference and a distinctive long tail also appeared in this case.

Figure 4 showed the solute plume of Brilliant Blue FCF through a rough single fracture with trapezoidal roughness. The differences from that shown in Figure 3 were as follows: the front of the plume was irregular, rather than smooth, which was obviously caused by the heterogeneity of fracture

wall roughness. Figure 4 also indicates that the solute concentration inside the plume was different and the solute migration rate was not the same for each point. In addition, retention of solute in some “dead-ends” caused by fracture wall roughness was clearly visible. Specifically, the retained solute was trapped for a long time in those dead-ends, leading to a long tail.

Figure 5 shows the solute plume through a rough single fracture with rectangular roughness. It is similar to Figure 4, with the exception that the irregularity degrees of plume were greater and the long tailing and solute-retention capacity were more pronounced.

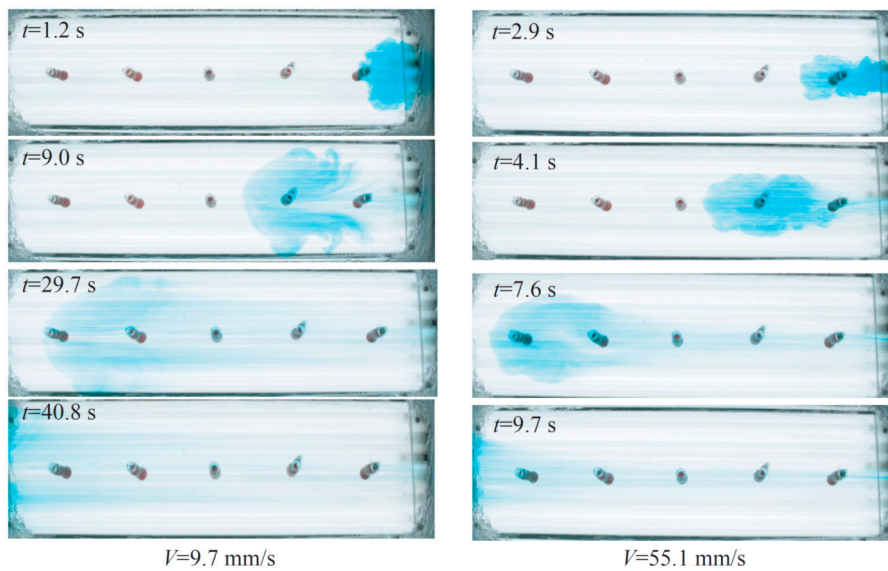


Figure 3. Solute plume of the tracer test in single fractures with smooth parallel plates.

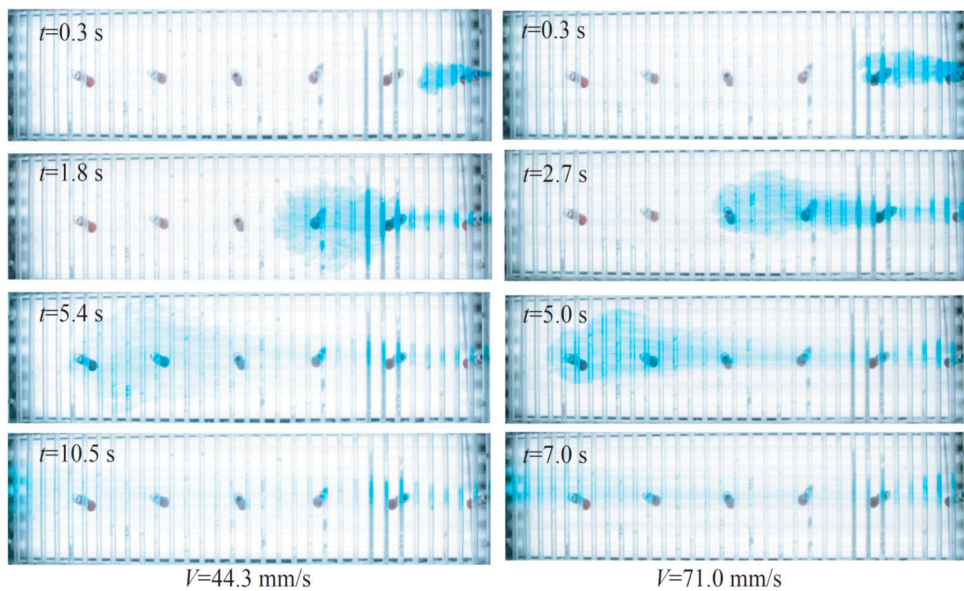


Figure 4. Solute plume of the tracer test in rough single fractures with rectangular roughness.

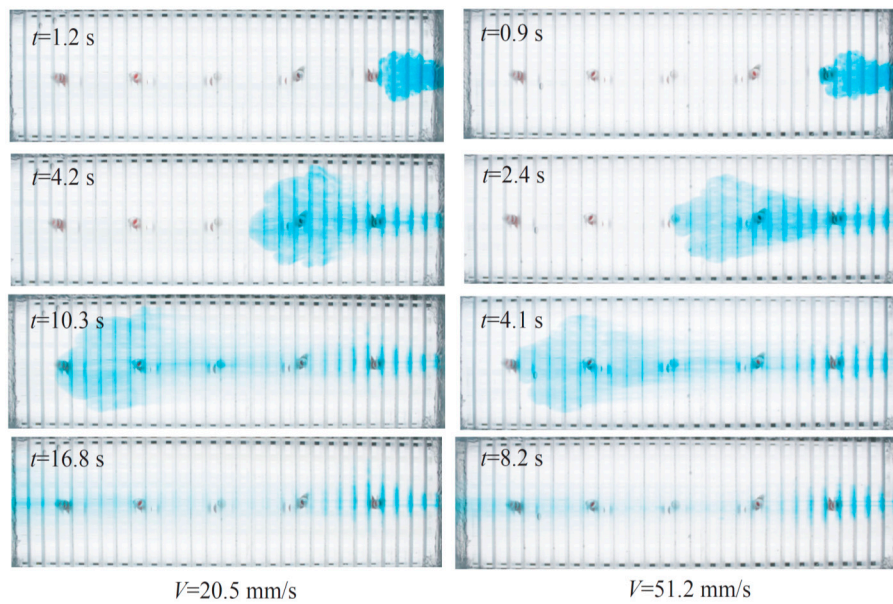


Figure 5. Solute plume of the tracer test in rough single fractures with trapezoidal roughness.

4. Interpretation of Experiments

In the following section, we seek to interpret the obvious non-Fickian transport phenomenon observed in Figures 3–5 using an appropriate theoretical model. Before discussing the transport process, it is necessary to address the flow process first as it was the fundamental driving force for hydrodynamic dispersion.

4.1. The Non-Darcian Equations

The experimental flow velocity–hydraulic gradient (V – J) relationships for different rough single fractures under different flow conditions are illustrated in Figures 6–8 and the fitting results, using linear Equation (1) and nonlinear Equations (2) and (3), and goodness of fit were also shown in Tables 3–5. Fitting parameters are listed in Table 6.

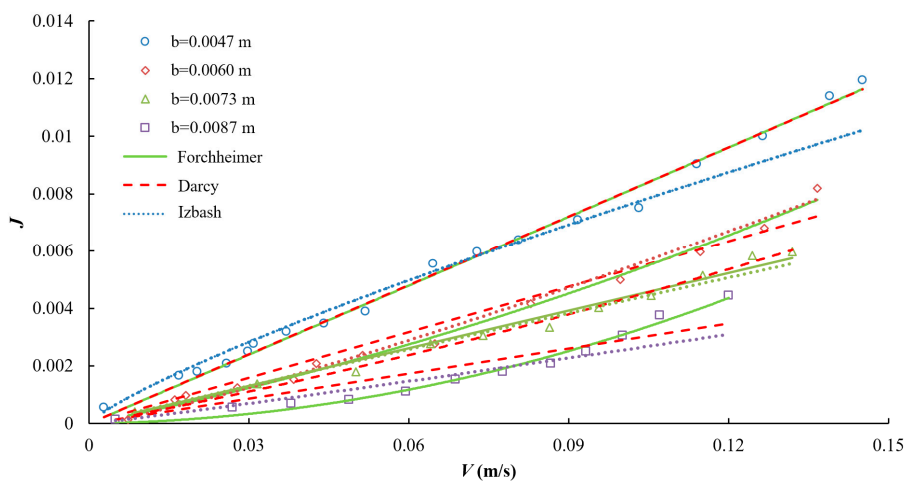


Figure 6. The V – J relationship and fitting results for flow through single fractures with smooth parallel plates.

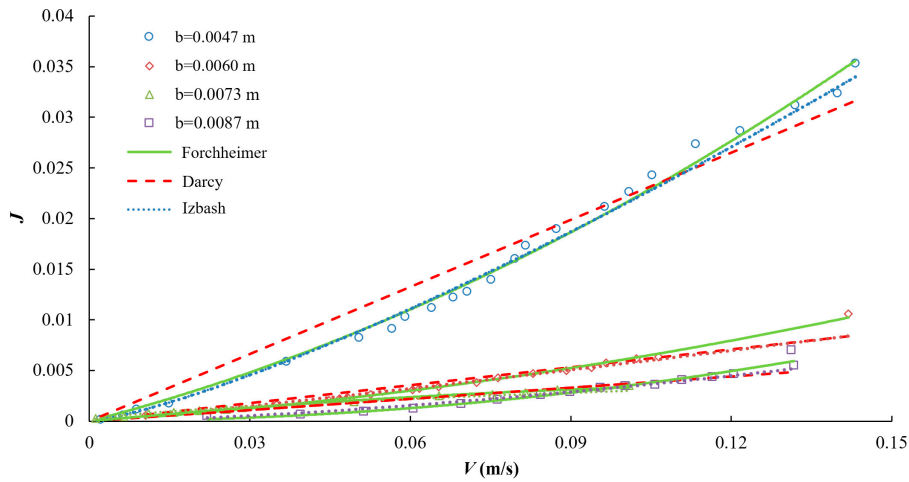


Figure 7. The V - J relationship and fitting results for flow through single fractures with rectangular roughness.

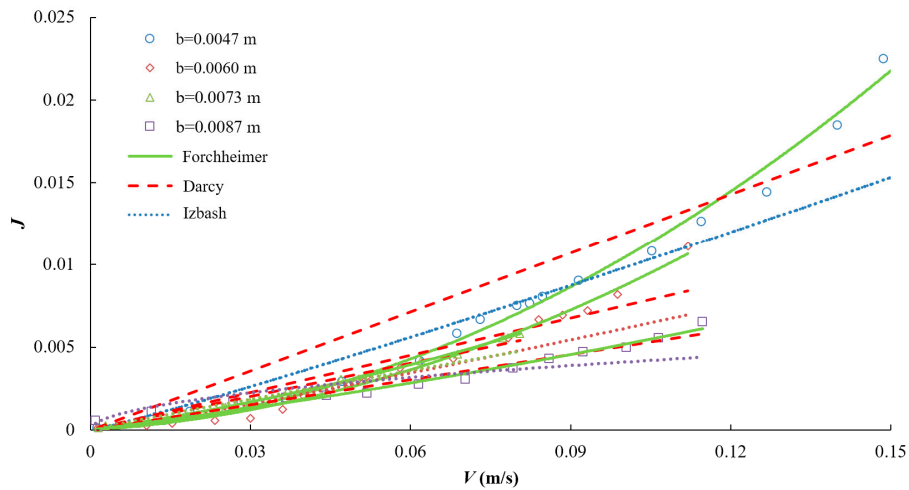


Figure 8. The V - J relationship and fitting results for flow through single fractures with trapezoidal roughness.

Table 3. Fitting results and goodness of fit for the V - J relationship for flow through single fractures with smooth parallel plates.

b (mm)	Re	Fitting Equations	r^2
4.7	20.0~1043.2	$J = 0.081V$	0.993
		$J = 0.049V^{0.813}$	0.977
		$J = 0.0036V^2 + 0.079V$	0.993
6.0	67.2~1253.7	$J = 0.052V$	0.974
		$J = 0.087V^{1.21}$	0.963
		$J = 0.14V^2 + 0.037V$	0.993
7.3	95.6~1472.4	$J = 0.043V$	0.981
		$J = 0.04V^{0.975}$	0.988
		$J = 0.084^2 + 0.034V$	0.991
8.7	15.0~1596.6	$J = 0.028V$	0.852
		$J = 0.031V^{1.07}$	0.937
		$J = 0.28^2 + 0.03V$	0.985

Table 4. Fitting results and goodness of fit for the V - J relationship for flow through single fractures with rectangular roughness.

b (mm)	Re	Fitting Equations	r^2
4.7	15.1~1021.1	$J = 0.22V$	0.96
		$J = 0.41V^{1.286}$	0.997
		$J = 0.78V^2 + 0.14V$	0.993
6.0	96.2~1300.0	$J = 0.059V$	0.925
		$J = 0.074V^{1.113}$	0.979
		$J = 0.33^2 + 0.0018V$	0.963
7.3	12.7~1131.1	$J = 0.037V$	0.948
		$J = 0.012V^{0.596}$	0.958
		$J = 0.27V^2 + 0.034V$	0.994
8.7	291.8~1743.8	$J = 0.037V$	0.809
		$J = 0.114V^{1.526}$	0.946
		$J = 0.16V^2 + 0.049V$	0.982

Table 5. Fitting results and goodness of fit for the V - J relationship for flow through single fractures with trapezoidal roughness.

b (mm)	Re	Fitting Equations	r^2
4.7	9.38~1097.4	$J = 0.12V$	0.864
		$J = 0.12V^{1.097}$	0.99
		$J = 0.82V^2 + 0.023V$	0.992
6.0	12.3~1025.6	$J = 0.075V$	0.89
		$J = 0.082V^{1.127}$	0.866
		$J = 0.67V^2 + 0.021V$	0.991
7.3	16.5~1114.2	$J = 0.067V$	0.981
		$J = 0.052V^{0.948}$	0.961
		$J = 0.31^2 + 0.047V$	0.996
8.7	12.1~1519.0	$J = 0.051V$	0.956
		$J = 0.013V^{0.499}$	0.869
		$J = 0.11^2 + 0.041V$	0.966

Table 6. Fitting parameters of non-Darcian equations.

Roughness Element	b (mm)	Darcy	Izbash		Forchheimer		Non-Darcian Coefficient
		k	c	m	a	b_c	β_c
Smooth parallel plates	4.7	0.081	0.049	0.813	0.079	0.0036	0.04
	6.0	0.052	0.087	1.21	0.037	0.14	1.37
	7.3	0.043	0.04	0.975	0.034	0.084	0.82
	8.7	0.028	0.031	1.07	0.03	0.28	2.74
Rectangular roughness	4.7	0.22	0.41	1.286	0.14	0.78	7.64
	6.0	0.059	0.074	1.113	0.0018	0.33	3.23
	7.3	0.037	0.012	0.596	0.034	0.27	2.65
	8.7	0.037	0.114	1.526	0.049	0.16	1.57
Trapezoidal roughness	4.7	0.12	0.12	1.097	0.023	0.82	8.04
	6.0	0.075	0.082	1.127	0.021	0.67	6.57
	7.3	0.067	0.052	0.948	0.047	0.31	3.04
	8.7	0.051	0.013	0.499	0.041	0.11	1.08

It was found that non-Darcian flow existed in both smooth and rough single fractures. The nonlinear phenomenon was more obvious in rough single fractures with high asperity heights,

which are the heights of roughness inside the fracture. The non-Darcian V – J relationships were best described by the Forchheimer equation.

The fitting parameters in Table 6 exhibited the following patterns. First, with the decrease of the asperity heights of the rough elements from 8 mm to 2 mm, the relative roughness (ε) decreased from 0.8 to 0.2 and the average aperture increased from 4.7 mm to 8.7 mm, the value of k in the Darcian equation decreased, indicating an increasing of permeability for the fracture. The value of c in the Izbash equation also decreased with the average aperture, but the value of m in the Izbash equation did not show any obvious trend. Second, fitting parameters showed different trends for smooth and rough single fractures. For smooth single fractures, the value of a in the Forchheimer equation decreased with the average aperture but the value of b_c and the value of the non-Darcian coefficient β_c increased with the average aperture. Third, the nonlinear phenomenon was more striking in smooth single fractures with larger average apertures. However, for rough single fractures in which flow can be described by the Forchheimer equation, a increased with the average aperture but b_c and β_c decreased with the average aperture. This was probably because the increase of asperity heights of rough elements in a rough single fracture would create greater fluid–solid contact surface, and enhance the frictional force for flow. Therefore, the relative importance of viscous flow versus inertial flow for a greater relative roughness is increased, reducing the flow nonlinearity (which is primarily caused by the inertial effect of flow).

4.2. The ADE and CTRW Models

The molecular diffusion coefficient D_m is set as $5.0 \times 10^{-11} \text{ m}^2 \cdot \text{s}^{-1}$ based on the Taylor–Aris experiment [1]. The Peclet numbers ($P_e = bV/D_m$) in our experiment were greater than 5×10^6 . As pointed out by Bauget and Fourar [1], when the Peclet number is greater than 4000, transverse dispersion can be ignored. The P_e numbers of our experiments were more than 100 times greater than 4000, which warranted the use of the one-dimensional approach. The CTRW Matlab Toolbox V3.1 [20] was employed for the CTRW TPL model.

BTCs at position $x = 555 \text{ mm}$ in single fractures with smooth parallel plates and rectangular rough single fractures were illustrated and fitted by ADE and CTRW TPL models. The results are shown in Figures 9 and 10 and Tables 7 and 8.

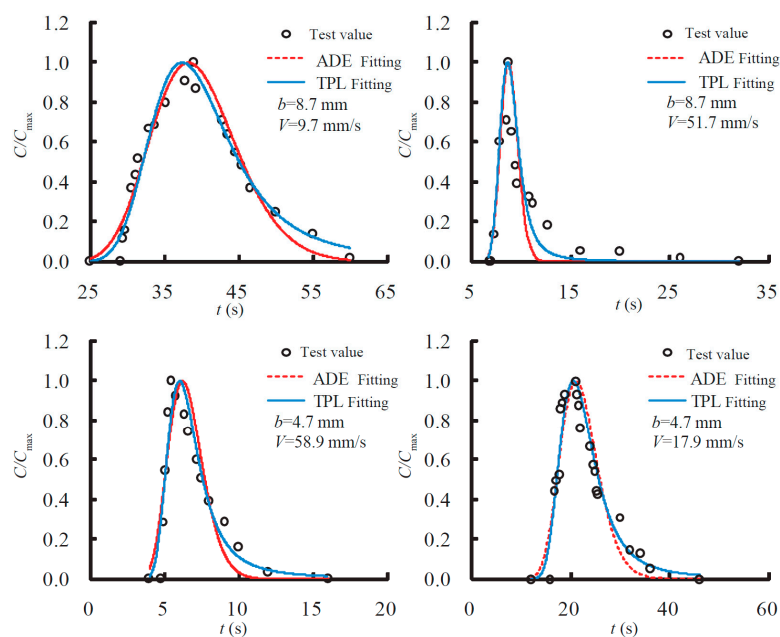


Figure 9. BTCs and fitting results in single fractures with smooth parallel plates ($x = 555 \text{ mm}$).

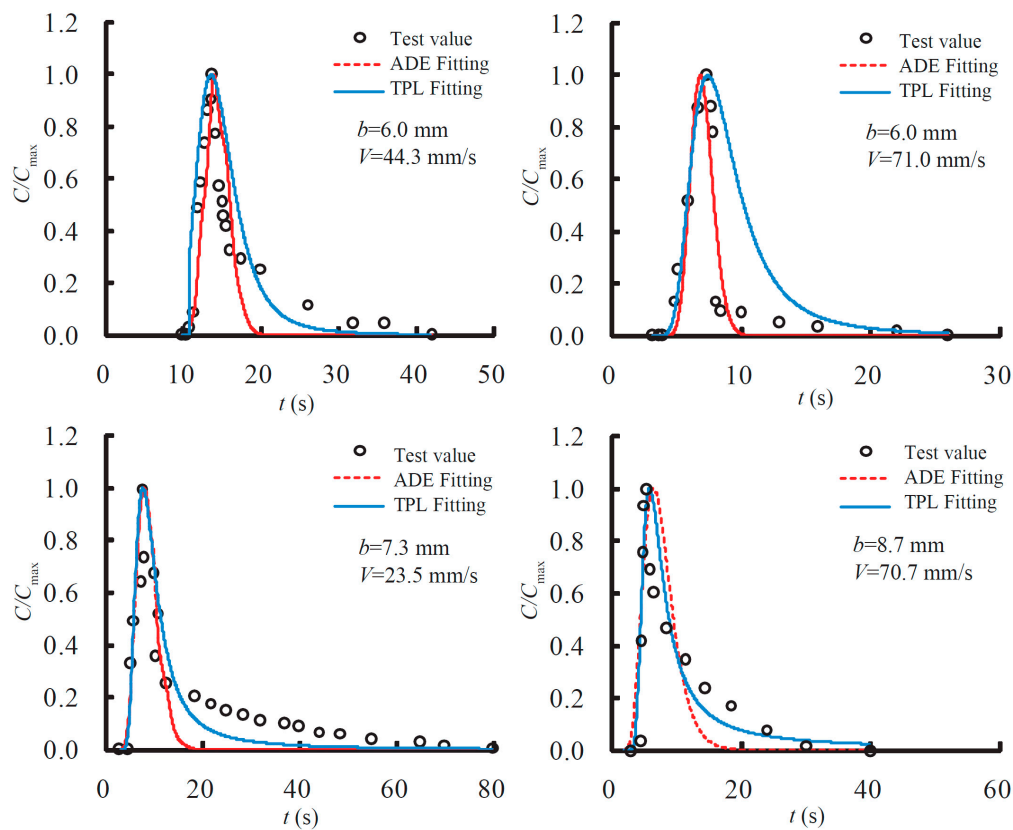


Figure 10. BTCs and fitting results in single fractures with rectangular rough fractures ($x = 555$ mm).

Table 7. Fitting parameters of BTC in single fractures with smooth parallel plates.

b mm	V mm/s	ADE				TPL							
		V_A mm/s	$D_A \times 10^{-4}$ m ² /s	r^2	RMSE	Lg(t_1)	Lg(t_2)	v_ψ mm/s	$D_\psi \times 10^{-4}$ m ² /s	β	r^2	RMSE	
4.7	17.9	25.2	2.16	0.932	0.165	-1.26	9.92	38.9	0.39	1.6	0.963	0.0895	
	58.9	84.8	8.0	0.891	0.172	-2.15	8.63	178.4	1.79	1.43	0.951	0.103	
8.7	9.7	14.0	0.86	0.943	0.133	-1.5	18.7	25.9	0.262	1.51	0.974	0.0537	
	51.7	62.5	1.72	0.924	0.172	-3.04	7.83	141.2	1.43	1.41	0.988	0.0428	

Table 8. Fitting parameters of BTC in single fractures with rectangular rough fractures.

b mm	V mm/s	ADE				TPL							
		V_A mm/s	$D_A \times 10^{-4}$ m ² /s	r^2	RMSE	Lg(t_1)	Lg(t_2)	v_ψ mm/s	$D_\psi \times 10^{-4}$ m ² /s	β	r^2	RMSE	
6.0	44.3	61.0	0.12	0.881	0.221	-2.62	8.6	365.2	3.72	1.05	0.962	0.121	
	71.0	71.9	0.21	0.904	0.157	-3.24	3.26	631.6	6.38	1.00	0.966	0.0895	
7.3	23.5	38.0	1.2	0.912	0.164	-1.01	9.75	41.3	0.43	1.87	0.957	0.185	
8.7	70.7	78.5	3.39	0.942	0.112	-1.71	4.34	112.3	1.45	1.7	0.985	0.0562	

We can make several interesting observations from Figures 9 and 10. First, BTCs followed the normal distribution in smooth single fractures, especially when the flow velocity was small. Second, as the flow velocity V increased, BTCs appeared to exhibit non-normal distributions with long tails. These non-normal distributions could be found ubiquitously in rough single fractures. Third, the classical ADE model was incapable of capturing the long-tailing of BTCs either in smooth or rough single fractures. However, the CTRW TPL model could better explain BTCs in both smooth and rough single fractures, especially in capturing the long-tailing phenomenon.

Similar conclusions can be obtained from Tables 7 and 8, as demonstrated by relatively smaller values of R^2 and larger RMSE values for the ADE model compared with the CTRW TPL model. The R^2 values were greater than 0.95 and the RMSE values were less than 0.1 with the CTRW TPL model, indicating satisfactory goodness of fit. It could be seen that the t_1 value in the CTRW TPL model was less than the observation time of the test and the t_2 value in the same model was much larger than the observation time of the test, indicating that the solute transport through single fractures under experimental flow conditions was far from reaching Fickian transport.

It can be seen from Tables 7 and 8 that $1 < \beta < 2$, reflecting how the solute transport in both smooth and rough single fractures under non-Darcian flow conditions had not reached Fickian migration. The β value decreased with the flow velocity and the relative roughness (ϵ), indicating that the degree of nonlinearity was stronger with larger flow velocity; and the degree of deviation from Fickian transport was also higher. Meanwhile, an increase of the asperity height would further aggravate the irregularity of solute transport. The above observations were made based on a β value of 1.05 and a ϵ value of 0.6 in single fractures with rectangular roughness.

In addition, the parameter v_ψ , which is the average velocity of solute particles in the CTRW TPL model, was much larger than the actual average velocity of V . This implied that the average velocity of solute particles was greater than the average velocity of flow.

To further study the effect of relative roughness (ϵ) on solute transport, BTCs at position $x = 355$ mm downstream, V of 71.0 m/s, b of 8.7 mm and 6.0 mm, and ϵ of 0.2 and 0.6 in single fractures with rectangular roughness were fitted by the CTRW TPL model; while BTCs at position $x = 355$ mm downstream, V of 49.5 m/s, b of 8.7 mm and 7.3 mm, and ϵ of 0.2 and 0.4 in single fractures with trapezoidal roughness were also fitted by the CTRW TPL model. The fitting results can be seen in Table 9. As a reference for comparison, BTCs at position $x = 355$ mm downstream, V of 59.0 m/s, and b of 4.7 mm and 8.7 mm in single fractures with smooth parallel plates were also fitted by the CTRW TPL and the results are also listed in Table 9.

Table 9. Fitting results of TPL for single fractures with different ϵ and b .

Roughness Element Structure	V mm/s	b mm	ϵ	TPL Fitting Parameters				
				v_ψ mm/s	$D_\psi \times 10^{-4}$ m ² /s	β	$\log_{10}(t_1)$	$\log_{10}(t_2)$
Rectangular	71.0	6.0	0.6	183.9	0.81	1.28	−0.746	11.257
		8.7	0.2	135.9	0.13	1.89	−1.291	1.210
Trapezoidal	49.5	7.3	0.4	256.4	0.26	1.19	−2.536	3.162
		8.7	0.2	98.6	0.57	1.67	−0.909	9.294
Smooth parallel plates	59.0	4.7	0	59.7	0.36	1.69	0.534	5.160
		8.7	0	131.2	0.13	1.70	−1.318	11.415

From Table 9, one can see that an increase of ϵ resulted in a significant reduction in the value of β ; that is, the degree of non-Fickian transport (or the deviation from Fickian transport) was affected significantly by ϵ in rough single fractures. However, the change of the b values in single smooth fractures had little effect on the value of β .

Furthermore, to analyze the effect of fracture roughness type (rectangular or trapezoidal) on solute transport, BTCs from rough single fractures with rectangular and trapezoidal roughness under the same flow condition ($V = 36.0$ mm/s) and the same ϵ value of 0.4 were fitted by the CTRW TPL model, and the results are shown in Table 10. As a reference for comparison, BTCs from smooth single fractures and rough single fractures with trapezoidal roughness under the same flow condition ($V = 51.5$ mm/s) and the same b value of 6 mm were fitted by the CTRW TPL model and the results are also listed in Table 10.

Table 10. Fitting results of the CTRW TPL model for single fractures with the same b with different roughness structure.

V mm/s	b mm	ε	Roughness Element Structure	TPL Fitting Parameters				
				v_ψ mm/s	$D_\psi \times 10^{-4}$ m ² /s	β	$\log_{10}(t_1)$	$\log_{10}(t_2)$
36.0	7.3	0.4	Rectangular	51.1	0.18	1.329	0.748	7.45
			Trapezoidal	110.8	0.11	1.469	−1.293	8.03
51.5	6.0	0.6	Trapezoidal	144.3	0.180	1.346	−1.334	5.26
		0	Smooth parallel plates	39.0	0.14	1.513	1.132	4.32

We can conclude from Table 10 that the β value under the same flow condition in a rough single fracture with a rectangular-type of roughness was smaller than that with a trapezoidal-type of roughness. As shown in Chen et al. [11], recirculation of flow in the eddies and curved streamline in a rough single fracture with the rectangular-type of roughness caused greater energy loss than that in the rough single fracture with a trapezoidal-type roughness. Such additional energy loss caused a greater degree of flow nonlinearity or stronger non-Darcian flow, leading to stronger non-Fickian transport and a smaller β value.

In summary, the heterogeneity of the fractured media, which is reflected in the relative roughness and roughness structure, was primarily responsible for the non-Fickian transport through rough single fractures. Also, the increase of flow nonlinearity of non-Darcian flow can exacerbate the non-Fickian transport phenomenon.

5. Conclusions

Artificial smooth and rough single fractures were constructed in the laboratory using organic glass plates. Compared with previous works focused on relatively low velocity and small apertures, medium aperture values ranging from 4.7 to 8.7 mm and the Reynolds numbers of 9.38–1743.8 were set to characterize the tracer transport through smooth and rough single fractures under non-Darcian flow conditions. The dye Brilliant Blue FCF was chosen as the tracer to facilitate the image process, enabling the solute transport process to be directly observed more intuitively.

It was found that non-Darcian flow existed in both smooth and rough single fractures under these experimental conditions. The nonlinear flow phenomenon was more obvious in rough single fractures, especially with large asperity heights. The non-Darcian flow velocity and hydraulic gradient (V – J) relationships were best described by the Forchheimer equation.

The classical ADE model was incapable of capturing the long-tailing of BTCs either in smooth or rough single fractures; the CTRW TPL model, with more adjustable parameters, can explain BTCs both in smooth and rough single fractures better, especially when it comes to capturing the long-tailing phenomenon.

The heterogeneity of the fractured media, which was manifested through the relative roughness and roughness structure, had a significant effect on the degree of deviation from Fickian transport (or the degree of non-Fickian transport) through rough single fractures. Also, the increase in the flow nonlinearity can further exacerbate the non-Fickian transport phenomenon. The non-Darcian coefficient β_c and the coefficient β in the CTRW TPL model seem to be good parameters for characterizing the heterogeneity of the rough fracture. The results may enhance our understanding of solute transport under non-Darcian flow conditions through fractured media. The study of solute transport and reactive transport through a real single fracture under non-Darcian conditions needs to be studied further.

Acknowledgments: The study is financially supported by the National Natural Science Foundation of China (Grant Nos. 41402197 and 41472233), the national key research and development plan (2016YFC0402807), and the Central University Fundamental Research Project of China (No. 26120132013B02914).

Author Contributions: Z.C. and H.Z. conceived and designed the experiments; G.Z. performed the experiments; Z.C. and H.Z. analyzed the data; Y.H. and Y.T. contributed reagents, materials and analysis tools; Z.C. wrote the paper and H.Z. revised the paper.

Conflicts of Interest: The authors declare no conflict of interest.

References

1. Bauget, F.; Fourar, M. Non-fickian dispersion in a single fracture. *J. Contam. Hydrol.* **2008**, *100*, 137–148. [[CrossRef](#)] [[PubMed](#)]
2. Berkowitz, B. Characterizing flow and transport in fractured geological media: A review. *Adv. Water Resour.* **2002**, *25*, 861–884. [[CrossRef](#)]
3. Dou, Z.; Zhou, Z.; Sleep, B.E. Influence of wettability on interfacial area during immiscible liquid invasion into a 3d self-affine rough fracture: Lattice boltzmann simulations. *Adv. Water Resour.* **2013**, *61*, 1–11. [[CrossRef](#)]
4. Dou, Z.; Zhou, Z.-F. Numerical study of non-uniqueness of the factors influencing relative permeability in heterogeneous porous media by lattice boltzmann method. *Int. J. Heat Fluid Flow* **2013**, *42*, 23–32. [[CrossRef](#)]
5. Wang, L.; Bayani Cardenas, M. Transition from non-fickian to fickian longitudinal transport through 3-d rough fractures: Scale-(in)sensitivity and roughness dependence. *J. Contam. Hydrol.* **2017**, *198*, 1–10. [[CrossRef](#)] [[PubMed](#)]
6. Becker, M.W.; Shapiro, A.M. Tracer transport in fractured crystalline rock: Evidence of nondiffusive breakthrough tailing. *Water Resour. Res.* **2000**, *36*, 1677–1686. [[CrossRef](#)]
7. Cherubini, C.; Giasi, C.I.; Pastore, N. Evidence of non-darcy flow and non-fickian transport in fractured media at laboratory scale. *Hydrol. Earth Syst. Sci.* **2013**, *17*, 2599–2611. [[CrossRef](#)]
8. Qian, J.; Zhan, H.; Chen, Z.; Ye, H. Experimental study of solute transport under non-darcian flow in a single fracture. *J. Hydrol.* **2011**, *399*, 246–254. [[CrossRef](#)]
9. Cvetkovic, V.; Haggerty, R. Transport with multiple-rate exchange in disordered media. *Phys. Rev. E* **2002**, *65*, 051308. [[CrossRef](#)] [[PubMed](#)]
10. Haggerty, R.; Gorelick, S.M. Multiple-rate mass transfer for modeling diffusion and. *Water Resour. Res.* **1995**, *31*, 2383–2400. [[CrossRef](#)]
11. Chen, Z.; Qian, J.; Zhan, H.; Zhou, Z.; Wang, J.; Tan, Y. Effect of roughness on water flow through a synthetic single rough fracture. *Environ. Earth Sci.* **2017**, *76*, 186. [[CrossRef](#)]
12. Bodin, J.; Delay, F.; De Marsily, G. Solute transport in a single fracture with negligible matrix permeability: 1. Fundamental mechanisms. *Hydrogeol. J.* **2003**, *11*, 418–433. [[CrossRef](#)]
13. Zimmerman, M.D.; Bennett, P.C.; Sharp, J.M., Jr.; Choi, W.-J. Experimental determination of sorption in fractured flow systems. *J. Contam. Hydrol.* **2002**, *58*, 51–77. [[CrossRef](#)]
14. Zhou, Q.; Liu, H.-H.; Bodvarsson, G.S.; Molz, F.J. Evidence of multi-process matrix diffusion in a single fracture from a field tracer test. *Transp. Porous Media* **2006**, *63*, 473–487. [[CrossRef](#)]
15. Cardenas, M.B.; Slottke, D.T.; Ketcham, R.A.; Sharp, J.M. Navier-stokes flow and transport simulations using real fractures shows heavy tailing due to eddies. *Geophys. Res. Lett.* **2007**, *34*. [[CrossRef](#)]
16. Cardenas, M.B.; Slottke, D.T.; Ketcham, R.A.; Sharp, J.M. Effects of inertia and directionality on flow and transport in a rough asymmetric fracture. *J. Geophys. Res.* **2009**, *114*, 258–266. [[CrossRef](#)]
17. Lee, S.H.; Yeo, I.W.; Lee, K.K.; Detwiler, R.L. Tail shortening with developing eddies in a rough-walled rock fracture. *Geophys. Res. Lett.* **2015**, *42*, 6340–6347. [[CrossRef](#)]
18. Cortis, A.; Berkowitz, B. Anomalous transport in “classical” soil and sand columns. *Soil Sci. Soc. Am. J.* **2004**, *68*, 1539–1548. [[CrossRef](#)]
19. Cortis, A.; Berkowitz, B. Computing “anomalous” contaminant transport in porous media: The ctw matlab toolbox. *Ground Water* **2005**, *43*, 947–950. [[CrossRef](#)] [[PubMed](#)]
20. Dentz, M.; Cortis, A.; Scher, H.; Berkowitz, B. Time behavior of solute transport in heterogeneous media: Transition from anomalous to normal transport. *Adv. Water Resour.* **2004**, *27*, 155–173. [[CrossRef](#)]
21. Geiger, S.; Cortis, A.; Birkholzer, J.T. Upscaling solute transport in naturally fractured porous media with the continuous time random walk method. *Water Resour. Res.* **2010**, *46*. [[CrossRef](#)]
22. Jiménez-Hornero, F.; Giráldez, J.; Laguna, A.; Pachepsky, Y. Continuous time random walks for analyzing the transport of a passive tracer in a single fissure. *Water Resour. Res.* **2005**, *41*, 1325–1327. [[CrossRef](#)]

23. Benson, D.A. The Fractional Advection—Dispersion Equation: Development and Application. Ph.D. Thesis, University of Nevada Reno, Reno, NV, USA, 1998.
24. Cherubini, C.; Giasi, C.I.; Pastore, N. On the reliability of analytical models to predict solute transport in a fracture network. *Hydrol. Earth Syst. Sci.* **2014**, *18*, 2359. [[CrossRef](#)]
25. Van Genuchten, M.T.; Wierenga, P.J. Mass transfer studies in sorbing porous media I. Analytical solutions. *Soil Sci. Soc. Am. J.* **1976**, *40*, 473–480. [[CrossRef](#)]
26. Moutsopoulos, K.N.; Koch, D.L. Hydrodynamic and boundary-layer dispersion in bidisperse porous media. *J. Fluid Mech.* **1999**, *385*, 359–379. [[CrossRef](#)]
27. Nowamooz, A.; Radilla, G.; Fourar, M.; Berkowitz, B. Non-fickian transport in transparent replicas of rough-walled rock fractures. *Transp. Porous Media* **2013**, *98*, 651–682. [[CrossRef](#)]
28. Wang, M.; Chen, Y.-F.; Ma, G.-W.; Zhou, J.-Q.; Zhou, C.-B. Influence of surface roughness on nonlinear flow behaviors in 3d self-affine rough fractures: Lattice boltzmann simulations. *Adv. Water Resour.* **2016**, *96*, 373–388. [[CrossRef](#)]
29. Wang, L.; Cardenas, M.B. Non-fickian transport through two-dimensional rough fractures: Assessment and prediction. *Water Resour. Res.* **2014**, *50*, 871–884. [[CrossRef](#)]
30. Iwai, K. Fundamental Studies of Fluid Flow through a Single Fracture. Ph.D. Thesis, University of California, Berkeley, CA, USA, 1976.
31. Lomize, G.M. *Flow in Fractured Rocks*; Gosenergoizdat: Moscow, Russia, 1951; pp. 127–129. (In Russian)
32. Qian, J.; Zhan, H.; Zhao, W.; Sun, F. Experimental study of turbulent unconfined groundwater flow in a single fracture. *J. Hydrol.* **2005**, *311*, 134–142. [[CrossRef](#)]
33. Novakowski, K.S.; Lapcevic, P.A.; Voralek, J.; Bickerton, G. Preliminary interpretation of tracer experiments conducted in a discrete rock fracture under conditions of natural flow. *Geophys. Res. Lett.* **1995**, *22*, 1417–1420. [[CrossRef](#)]
34. Chen, Z.; Qian, J.-Z.; Qin, H. Experimental study of the non-darcy flow and solute transport in a channeled single fracture. *J. Hydrodyn.* **2011**, *23*, 745–751. [[CrossRef](#)]
35. Qian, J.Z.; Chen, Z.; Zhan, H.B.; Luo, S.H. Solute transport in a filled single fracture under non-darcian flow. *Int. J. Rock Mech. Min.* **2011**, *48*, 132–140. [[CrossRef](#)]
36. Bear, J. *Dynamics of Fluids in Porous Media*; Courier Corporation: North Chelmsford, MA, USA, 2013.
37. Ranjith, P.G.; Darlington, W. Nonlinear single-phase flow in real rock joints. *Water Resour. Res.* **2007**, *43*. [[CrossRef](#)]
38. Bear, J. *Dynamics of Fluids in Porous Materials*; Society of Petroleum Engineers: Dallas, TX, USA, 1972.
39. Berkowitz, B.; Cortis, A.; Dentz, M.; Scher, H. Modeling non-fickian transport in geological formations as a continuous time random walk. *Rev. Geophys.* **2006**, *44*. [[CrossRef](#)]
40. Berkowitz, B.; Kosakowski, G.; Margolin, G.; Scher, H. Application of continuous time random walk theory to tracer test measurements in fractured and heterogeneous porous media. *Ground Water* **2001**, *39*, 593–604. [[CrossRef](#)] [[PubMed](#)]
41. Berkowitz, B.; Scher, H. Theory of anomalous chemical transport in random fracture networks. *Phys. Rev. E* **1998**, *57*, 5858–5869. [[CrossRef](#)]
42. Berkowitz, Y.; Edery, Y.; Scher, H.; Berkowitz, B. Fickian and non-fickian diffusion with bimolecular reactions. *Phys. Rev. E* **2013**, *87*. [[CrossRef](#)]
43. Persson, M. Accurate dye tracer concentration estimations using image analysis. *Soil Sci. Soc. Am. J.* **2005**, *69*, 967. [[CrossRef](#)]
44. Forrer, I.; Papritz, A.; Kasteel, R.; Flüher, H.; Luca, D. Quantifying dye tracers in soil profiles by image processing. *Eur. J. Soil Sci.* **2000**, *51*, 313–322. [[CrossRef](#)]

